



Heterophase fluctuations near T_c in the relaxor ferroelectrics $(1-x)\text{Pb}(\text{Zn}_{1/3}\text{Nb}_{2/3})\text{O}_3-x\text{PbTiO}_3$ ($x = 0.09$) studied by x-ray diffuse scattering and coherent x-ray scattering

Kenji Ohwada,^{1,2,*} Jun'ichiro Mizuki,^{1,2,3} Mitsuyoshi Matsushita,^{2,4} and Kazumichi Namikawa^{2,5}

¹Quantum Beam Science Center (SPring-8), Japan Atomic Energy Agency, 1-1-1 Kouto, Sayo-cho, Sayo-gun, Hyogo 679-5148, Japan

²CREST, Japan Science and Technology Agency (JST), Kawaguchi, Saitama 332-0012, Japan

³School of Science and Technology, Kwansai Gakuin University, 2-1 Gakuen, Sanda, Hyogo 669-1337, Japan

⁴Functional Materials Development Center, Research Laboratories, JFE Mineral Co., Ltd., 1 Nishihama, Chuou-ku, Chiba, Chiba 260-0826, Japan

⁵Tokyo Gakugei University, 4-1-1 Nukuikita-machi, Koganei, Tokyo 184-8501, Japan

(Received 9 June 2014; published 29 September 2014)

The paraelectric (PE) to ferroelectric (FE) first-order phase transition of $(1-x)\text{Pb}(\text{Zn}_{1/3}\text{Nb}_{2/3})\text{O}_3-x\text{PbTiO}_3$ ($x = 0.09$) ($T_c^c = 455$ K on cooling) has been studied by the complementary use of x-ray diffuse scattering (XDS) and coherent x-ray scattering (CXs). XDS was mainly used to investigate the FE regions, while CXs was mainly used to investigate the PE regions above T_c^c on cooling. The diffuse scattering intensity due to the appearance of FE regions shows a maximum at $T_{\text{max}} = 460$ K. The diffuse scattering is dynamic in nature and the softening trend changes to a hardening trend at T_{max} . This means that the FE instability is maximum at T_{max} and therefore the FE regions are well stabilized below T_{max} . The spatial autocorrelation function obtained by CXs, corresponding to the texture of PE regions, starts to rapidly change at about T_{max} and is most unstable at T_c^c . We conclude that a heterophase fluctuation occurs between T_c^c and T_{max} near the phase transition. The heterophase fluctuation can be expected to correlate to the low-frequency dielectric dispersion and contribute to the phase transition as a precursor phenomenon of the first-order phase transition.

DOI: [10.1103/PhysRevB.90.104109](https://doi.org/10.1103/PhysRevB.90.104109)

PACS number(s): 61.05.C-, 77.80.Jk, 77.80.B-, 77.90.+k

I. INTRODUCTION

Relaxors are characterized by a number of unique properties, many of which are not fully understood. The dielectric constant $\varepsilon(T)$ exhibits a large broad peak around T_{max} . ε and T_{max} strongly depend on the frequency of the external field, which indicates a *relaxation* process with multiple time scales. For nearly half a century after the discovery of relaxors [1], considerable attention was paid to lead-based perovskite relaxors because they often exhibit colossal dielectric and piezoelectric responses, which are of interest in both scientific research and industrial applications. Despite long and intensive research, arguments about the intrinsic mechanism underlying the unique properties of lead-based relaxors are still unsettled. One of the main reasons is that it is necessary to deal with the nanometer- to micrometer-scale heterogeneity (or heterophase) [2,3] intrinsic to relaxors.

In some cases, *heterogeneity* contributes to an extremely large susceptibility in solids. It is generally accepted that the relaxor properties are associated with the so-called polar nanoregions (PNRs) that grow in a paraelectric (PE) matrix, whose existence was originally proposed by Burns and Dacol [4,5] through measurements of the refraction indices $n(T)$ of the perovskite-type oxides $\text{Pb}(\text{Zn}_{1/3}\text{Nb}_{2/3})\text{O}_3$ (PZN) and $\text{Pb}(\text{Mg}_{1/3}\text{Nb}_{2/3})\text{O}_3$ (PMN). Colossal magnetoresistance (CMR) phenomena are observed in perovskite-type hole-doped manganites. The CMR properties are due to the phase competition between a double-exchange ferromagnetic metal phase and a charge-orbital-ordered antiferromagnetic phase [6]. The engineered domain structure [7] in ferroelectrics is well known to enhance piezoelectric responses [8]; further-

more, the smaller the ferroelectric (FE) domain size, the better [9]. The mechanism of the enhancement has been suggested to be comprehensible within the framework of the coexistence of stable and metastable phases associated with the first-order phase transition near the morphotropic phase boundary (MPB) [10]. The superelasticity effect in martensite alloys can also be understood from this viewpoint.

One of the keys to understanding the formation of such a wide variety of heterogeneous structures is the first-order phase transition near the critical point. Actually, relaxor systems exist near the critical end point [11,12], while CMR appears near the bicritical point [6]. The length scale of heterogeneous structures is distributed from nanometers to micrometers [3,6]. The variation in length scale is due to a variation in the effects of randomness, intentionally doped impurities, strain fields, and so forth. Under these circumstances, the importance of understanding the relationship between heterogeneous structures extending over a wide range of length scales and the resulting bulk physical properties is increasing.

Previously, for this purpose, we proposed a multiple-length-scale approach [13] intended for research on FEs, which involved the complementary use of coherent x-ray scattering (CXs), x-ray diffuse scattering (XDS), conventional x-ray diffraction techniques, and dielectric measurements. The cubic (PE) to tetragonal (FE) first-order phase transition of $(1-x)\text{Pb}(\text{Zn}_{1/3}\text{Nb}_{2/3})\text{O}_3-x\text{PbTiO}_3$ ($x = 0.09$) (PZN-9%PT), a solid solution of the relaxor PZN and PbTiO_3 (PT) near the MPB concentration [8], was investigated by this approach.

Figure 1 shows the temperature dependencies of (a) the lattice constants and (b) the dielectric permittivity of PZN-9%PT for various frequencies [13]. It is clear that the phase transition takes place at 455 K (T_c^c) on cooling but at 459 K (T_c^h) on heating. In this paper, we focus on the cooling process. The dielectric constant reaches a maximum at 459 K and

*ohwada@spring8.or.jp

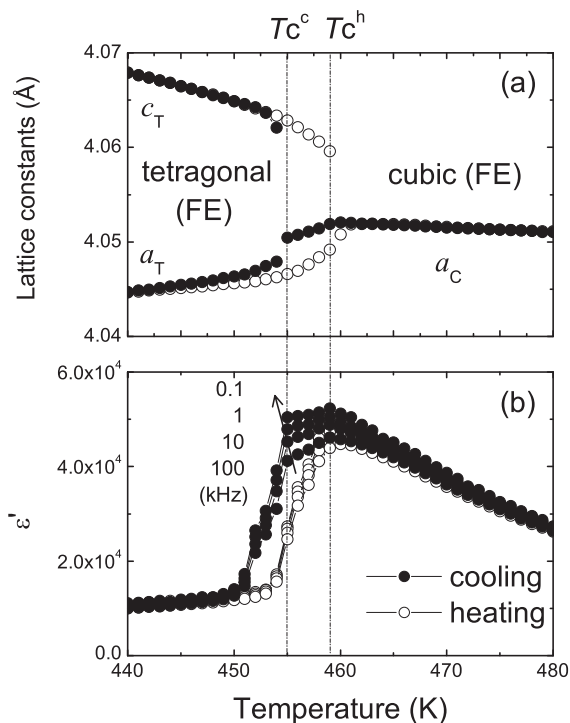


FIG. 1. Temperature dependencies of the (a) lattice constants and (b) dielectric permittivity of PZN-9%PT for various frequencies [13]. Solid and open circles represent cooling and heating, respectively.

starts to decrease toward T_C^c . The dependence on frequency is obvious between the two characteristic temperatures. Intermediate submicrometer structures were suggested to contribute directly to the frequency dependence and the phase transition [13]. However, the details were unclear owing to a lack of experimental accuracy. In particular, in the CXS results, the measurement time was extremely long and the physical picture in the case of cooling toward T_C^c was highly speculative.

In this paper, we revisit the phase transition of PZN-9%PT and precisely study how the submicrometer-scale heterogeneous structure evolves and contributes to the physical properties as well as the phase transition. For this purpose, XDS and CXS measurements were used as a complementary approach to consider the heterogeneity. In this new study, we apply an improved CXS method and perform a more quantitative analysis of both the XDS and CXS results. Since we trace the appearance and growth process of FE regions in the PE phase on cooling toward T_C^c , the CXS pattern closely reflects the PE regions segmentalized by the newly appearing FE regions, while the XDS pattern closely reflects the newly appearing FE regions.

From the viewpoint of developing the use of coherent x rays in the field of solid-state physics, the present problem, i.e., the contribution of the submicrometer-scale heterogeneous structure to the phase transition requires a suitable experimental system. A general framework for the present coherent/partially coherent x-ray scattering is given in Appendices A and B, along with an interpretation of the present CXS results. The present CXS method is a different type of application of coherent x rays from x-ray photon correlation spectroscopy

(x-ray intensity fluctuation spectroscopy) [14,15] and coherent diffraction imaging [16,17].

II. EXPERIMENT

A. Sample preparation

We prepared a $10 \times 10 \times 0.25 \text{ mm}^3$ wafer of PZN-9%PT with a PT concentration gradient of as low as $<0.02\%/ \text{mm}$ from a large single crystal grown by JFE Mineral Co., Ltd. [18]. The wafer was cut to expose the (100) plane.

To perform dielectric measurement and x-ray measurement simultaneously, two rectangular electrodes were evaporated parallel to each other on the surface of the wafer with a gap of $200 \mu\text{m}$. Gold wires were connected to the electrodes as shown in Fig. 2(a). The dielectric permittivity was measured between the two electrodes, while x rays interacted with the sample only in the $200 \mu\text{m}$ gap, as shown in Fig. 2(a), which enabled us to verify that we were precisely monitoring the structure that contributed to the dielectric properties. The dielectric permittivity was derived from capacitance measurements using an LCR meter (Wayne Kerr 6400B). Dielectric measurements were stopped during x-ray measurements to eliminate the effects of ac electric fields. The dielectric permittivity shown in Fig. 1(b) [13] was reproduced.

The sample was mounted on a MicrostatHiResII stage (Oxford Instruments). In the present experiment, the temperature was controlled to within $\pm 0.04 \text{ K}$ between 480 and 440 K.

B. X-ray scattering measurements

X-ray scattering measurements were performed at BL22XU of SPring-8 [19]. The x rays from an in-vacuum undulator were monochromatized by a liquid-nitrogen-cooled Si(111) double-crystal monochromator. The energy was tuned to 9 keV ($\lambda = 1.378 \text{ \AA}$). As shown in Fig. 3, the monochromatized x rays were collimated by the upstream aperture (A_1) to a certain size and guided to the $200 \mu\text{m}$ gap between the two electrodes (see Fig. 2). The scattered x rays were measured using the combination of a receiving aperture (A_2) and a detector (D). The distances from A_1 to the sample (S) and from S to A_2 were 0.15 m ($=R_1$) and 1.2 m ($=R_2$), respectively.

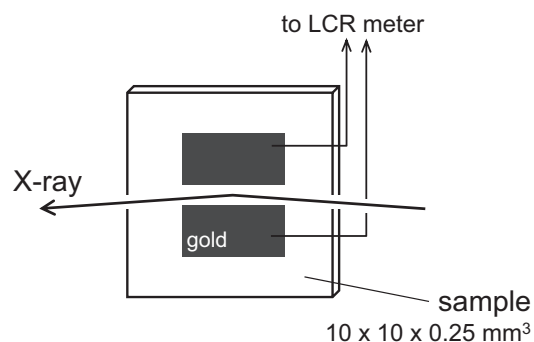


FIG. 2. A $10 \times 10 \times 0.25 \text{ mm}^3$ wafer of PZN-9%PT. Two rectangular electrodes were evaporated parallel to each other on the surface with a gap of $200 \mu\text{m}$. X rays are targeted at a location between the two electrodes, enabling simultaneous x-ray scattering and dielectric measurements.

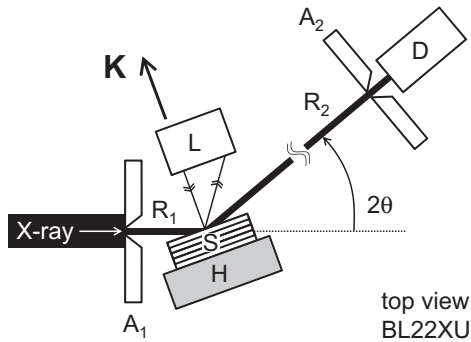


FIG. 3. Top view of optical alignment for x-ray scattering measurements at BL22XU of SPring-8. A_1 , upstream aperture; A_2 , receiving aperture; S, sample; H, sample holder; D, detector; \mathbf{K} , scattering vector; and L, displacement sensor. R_1 and R_2 are the distances from A_1 to S and from S to D (or A_2), respectively.

1. XDS measurement

For the XDS measurement, A_1 was set to $60 \times 60 \mu\text{m}^2$, while A_2 was set to $1 \times 1 \text{mm}^2$. These were the conditions for measurements using partially coherent x rays to obtain information on the fluctuation of solids [see Appendix A, Eqs. (A6) and (A7)]. An avalanche photodiode (APD) was used as the detector.

2. CXS measurement

For the CXS measurement [20,21], A_1 was set to $10 \times 10 \mu\text{m}^2$ (a^2), while A_2 was fully opened. A high-resolution x-ray CCD camera was used for the precise measurement of coherent x-ray “speckle” scattering patterns (see Appendix A). We selected a high resolving power at the cost of sensitivity, and thus used Lu_2SiO_5 (LSO) as a scintillator, since its thickness can be reduced to $10 \mu\text{m}$. The thin LSO makes it possible to reduce diffusion, providing us with a clear image. By coupling a microscope and an ORCA-HR CCD camera (Hamamatsu Photonics K.K.), we obtained a spatial resolution of $5.9 \mu\text{m}$ full width at half maximum. The scintillator was placed at a distance of 1.4 m from the sample ($R_2 = 1.4 \text{m}$ in this case). R_1 satisfied the near-field condition ($R_1 \ll a^2/\lambda$), while R_2 satisfied the far-field condition ($R_2 \gg a^2/\lambda$). $R_1 \ll a^2/\lambda$ ensures that the incident x ray is a pseudoplane wave at the sample position, while $R_2 \gg a^2/\lambda$ ensures that the diffracted x ray exhibits far-field diffraction, where the speckle patterns show a similar shape even when R_2 is changed.

Since the speckle pattern is sensitive to the heterogeneity in the irradiated area, and therefore sensitive to where the x ray irradiates the sample (see Appendix A), it is necessary to know how the sample moves as its temperature changes. By considering the expansion/contraction of the sample holder (H), the sample mostly moves along the scattering vector (\mathbf{K}). As shown in Fig. 3, a displacement sensor (L: Keyence LK-G402) was placed in front of the sample and the temperature dependence of the sample position along the scattering vector,

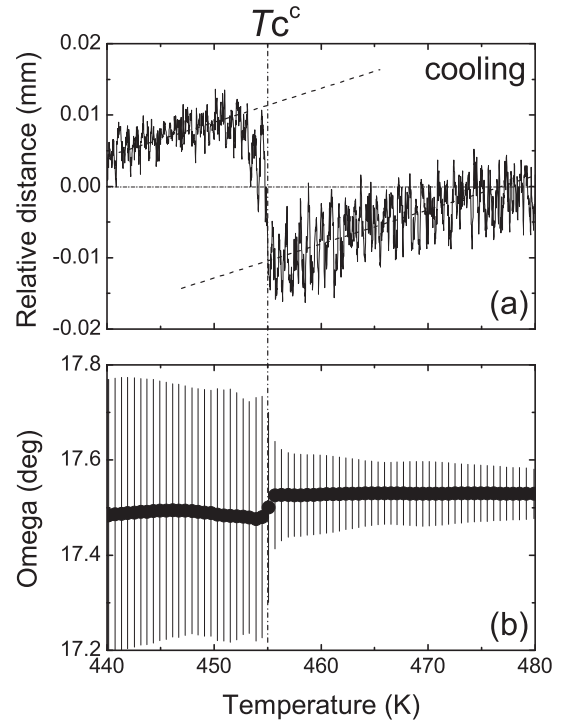


FIG. 4. Temperature dependencies of (a) relative distance and (b) peak position (solid circles) and width (bars) of rocking curve.

i.e., the distance from the sensor to the sample (S-to-L relative distance), was measured with a resolution of $2 \mu\text{m}$.

Figure 4(a) shows the measured S-to-L relative distance. It gradually decreases as the temperature decreases and rapidly increases at T_c^c . After the phase transition, it continues to decrease. The sudden change at T_c^c shows that macroscopic strain was induced by the PE to FE phase transition. As shown by the dotted lines, the rate of decrease is constant and the same before and after the phase transition. This means that the sample stage moves in a straight line as its temperature changes and that the trend is constant in the temperature range across the PE to FE phase transition.

Figure 4(b) shows the temperature dependencies of the peak position of the 200 Bragg reflection (solid circles) and width (bars) of the rocking curve of PZN-9%PT. The peak position is almost constant and the change is negligible compared with the peak width of the PE regions above T_c^c .

From the results shown in Figs. 4(a) and 4(b), we could measure the CXS patterns from PZN-9%PT by only changing the temperature and using the same scattering condition between 480 and 455 K (PE phase). We successfully obtained 442 frames of the speckle pattern at the 200 Bragg position between 480 and 455 K. The exposure time in the present measurement was 1 min for each frame and the cooling rate was 3.33 K/h; therefore, the temperature interval of the measurements was about 0.06 K/frame. As shown in Appendix B, the speckle pattern clearly reflects the texture of the PE regions contributing to the scattering in the coherently irradiated area. Analysis of the CXS results was performed using IMAGEJ software [22].

III. RESULTS

A. X-ray diffuse scattering from ferroelectric regions

Figure 5 shows the mesh scan results around the 200 Bragg point taken at (a) 460 K [13] and (b) 480 K. Diffuse scattering was clearly observed and the intensity distribution was maximum near the Γ point. We also show the difference in the intensities between the two sets of data in Fig. 5(c). The diffuse scattering intensity increases in area A but not in area B [see Fig. 5(c)]. This means that the *transverse*-wave-like fluctuation is the dominant cause of the diffuse scattering near T_c . These results suggest that the ferroelectric and/or ferroelastic correlation increases on cooling.

Figure 6 shows the peak profile taken along $(2+h, -h, 0)$ ($-0.005 \leq h \leq 0.05$) at 480 K. The intensity changes by a factor of 10^7 and is shown on a logarithmic scale. The resolution of the present scattering condition is also shown. The profile is also shown on a linear scale in the inset. The strong central peak represents Bragg reflection, while the weak and broad tail represents diffuse scattering. The boundary between the two types of scattering cannot be clearly seen; however, their temperature dependencies enable them to be clearly separated.

We obtained the temperature dependence of the x-ray scattering intensity at several positions ($h = 0, 0.005$ [13], 0.01, 0.02, 0.03, and 0.05), as indicated by arrows in Fig. 6 (white circles in Fig. 5). The results are shown in Fig. 7. The background level was about 0.5 cps ($=30$ counts/60 s) and negligible in all the measurements.

The intensity at the Γ point ($h = 0$) tends to decrease toward T_c^c , while the intensities away from the Γ point ($h = 0.005$ – 0.05) tend to increase toward 460 K ($=T_{\max}$),

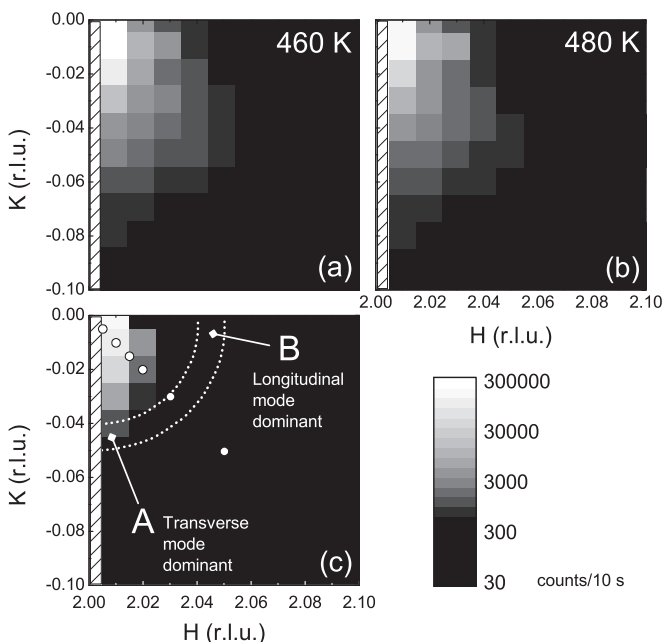


FIG. 5. Diffuse scattering distribution around the 200 Bragg point taken at (a) 460 K [13] and (b) 480 K. (c) Intensity difference between 460 and 480 K ($I_D^{460\text{K}} - I_D^{480\text{K}}$). An increase in the diffuse scattering intensity is clearly seen around area A, which means that the transverse-wave-like fluctuation is the dominant cause of the diffuse scattering near T_c .

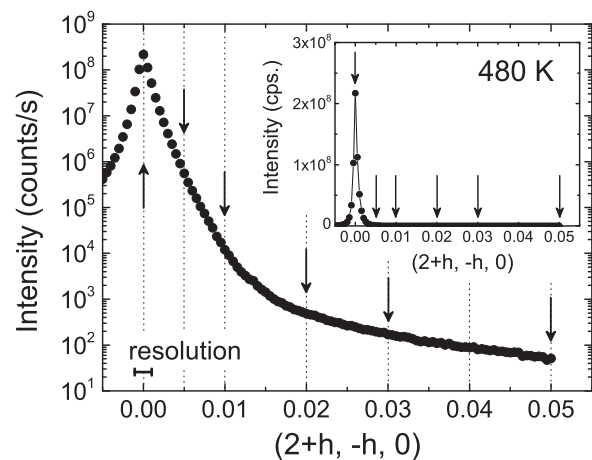


FIG. 6. Peak profile taken along $(2+h, -h, 0)$ ($-0.005 \leq h \leq 0.05$) at 480 K shown on a logarithmic scale. The inset shows the results plotted on a linear scale.

then decrease toward T_c^c and finally rapidly decrease below T_c^c . The results also show that the tail of intense Bragg reflection does not affect the diffuse scattering even at $h = 0.005$. The decrease in the Bragg intensity also closely corresponds to the increase in the width of the rocking curve [see Fig. 4(b)].

One can clearly see from the sequential measurements in Fig. 7 that the anomaly of the diffuse scattering intensity toward T_c^c becomes unclear as h increases but that it retains a similar shape. The present h dependence shows that the properties cannot *simply* be explained by the effect of increasing or decreasing scatterer density causing the diffuse scattering, or by the effect of an increasing FE correlation length. The former case would indicate that all the diffuse data from Figs. 7(b)–7(f) should be normalized by a single parameter, while the latter case would result in a different T_{\max} depending on the h value.

As discussed in Appendix A, the diffuse scattering closely reflects the fluctuation of solids as shown in Eq. (A3). Meanwhile, as already pointed out in Ref. [13], the temperature dependence of the diffuse scattering intensity [see Fig. 7(b)] closely resembles the temperature dependence of the dielectric constant on the high-frequency side [see Fig. 1(b), 100 KHz]. This clearly indicates that the diffuse scattering originates from the fluctuation-dissipation theorem, the diffuse scattering intensity is proportional to the real part of the ionic susceptibility [$\chi_{\text{ion}}(\mathbf{K}, \omega)$], i.e., $I_D(\mathbf{K}) \propto \chi'_{\text{ion}}(\mathbf{K}, 0)$, where all the ionic-dynamic contributions are integrated.

We suppose here that the diffuse scattering is mainly dynamic in nature. In this case, the transverse acoustic (TA) phonon mode, which is the lowest-energy phonon mode, probably mainly determines the diffuse scattering intensity. Under this supposition, the diffuse scattering intensity should be inversely proportional to the square of the frequency of the TA mode as $I_D(q) \propto 1/\omega_{TA}^2(q)$.

Using this relation, we calculated $(1/I_D)^{1/2}$ at all the h positions for selected temperatures of 480, 460, and 440 K as shown in Fig. 8. A straight line passing through the origin is also shown as a guide to the eye. It can be seen that the

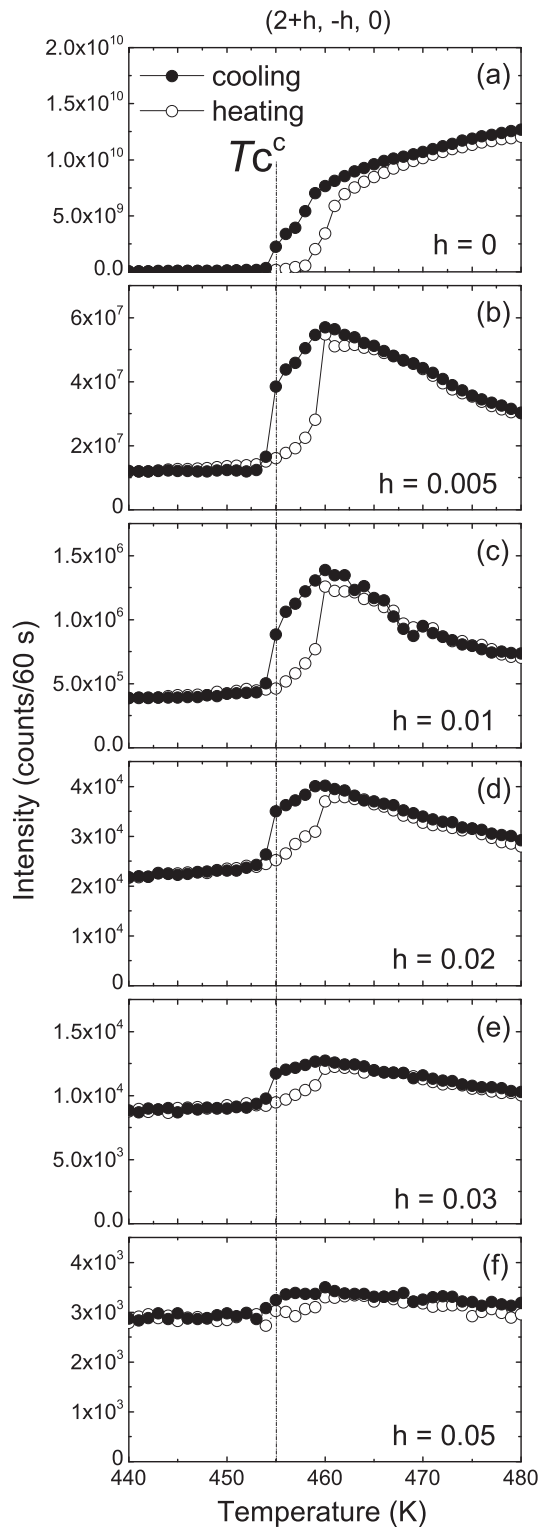


FIG. 7. Temperature dependence of the scattering intensity at $h =$ (a) 0, (b) 0.005 [13], (c) 0.01, (d) 0.02, (e) 0.03, and (f) 0.05.

$h - (1/I_D)^{1/2}$ relation can be separated into two regions on either side of $h = 0.015$.

The linear relation in the high- h region between 0.02 and 0.05 thoroughly supports the validity of the supposition that the diffuse scattering mainly originates from the TA mode (ω_{TA}).

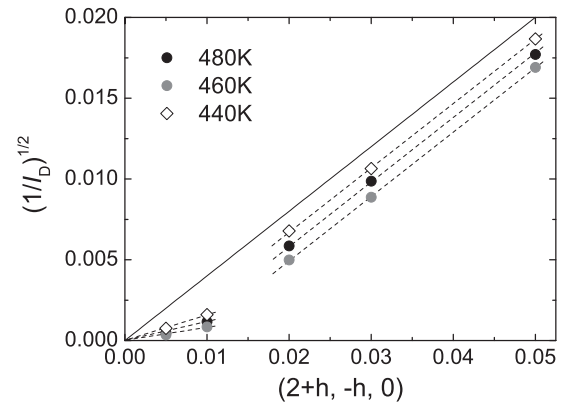


FIG. 8. $(1/I_D)^{1/2}$ at all h positions for selected temperatures of 480, 460, and 440 K.

This is because, generally speaking, the dispersion relation of the acoustic mode is approximately linear near the Γ point as $\omega_{TA} \propto h$. On the other hand, in the low- h region between 0 and 0.01, a change in the slope with the temperature was observed. A similar phenomenon was observed as TA-mode softening in the Jahn-Teller material PrAlO_3 [23]. However, since the acoustic mode is the *strain* mode, the TA mode alone cannot explain the similarity in the temperature dependence between the diffuse scattering intensity and the high-frequency dielectric constant. We have to consider other contributions as well as TA-mode softening (or damping).

The transverse optic (TO) mode is the most probable polarization mode. The contribution of the TO mode to the diffuse scattering near the Γ point has been suggested for many relaxor ferroelectrics [24–29]. The frequency of the TO mode is usually much higher than that of the TA mode near the Γ point and these modes are difficult to detect by XDS. However, once the polar regions are formed by TO-mode condensation/damping, the contribution of the polarization becomes detectable by XDS. Strictly speaking, for the formation of polarization and the related TO-mode condensation/damping, the contribution of the random Pb displacement at the perovskite A site, a structural characteristic of Pb-based relaxors, is important [30–34]. However, we do not go into this in detail in this paper.

Once the polar regions are formed, they behave as dynamic pseudospins at high temperatures and the coupling between the pseudospin relaxational mode and the TA phonon mode should be activated [35], which results in quasielastic scattering [29,36]. Such coupling was experimentally verified in PMN-30%PT (near the MPB composition) [37]. In our PZN-9%PT sample, the TA-mode softening (or damping) associated with the coupling with polarization takes place at a very low h as shown in Fig. 8.

On the basis of the dynamic nature of the diffuse scattering, the most important point of the present results is that the hardening trend starts at T_{\max} . The value of $h \sim 0.015$ should correspond to the smallest size of the polar regions coupling to the TA mode in this material. Therefore, the size of the polar regions, i.e., the FE regions, is estimated to be larger than 20 nm.

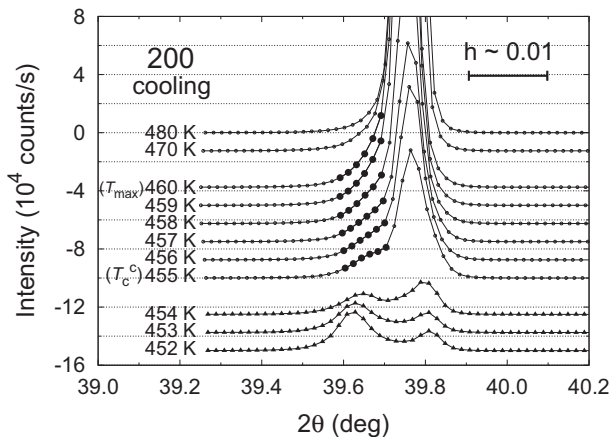


FIG. 9. Temperature dependence of 2θ - ω profiles across the 200 Bragg reflection.

Figure 9 shows the results of longitudinal scans across the 200 Bragg point (2θ - ω profiles) as a function of temperature. As shown by the filled circles, the tail of the 200 Bragg reflection on the low-angle side develops toward T_{\max} , while it starts to form a Bragg peak corresponding to the FE phase toward T_c . These features closely correspond to the results of XDS presented in this section, and the size of the FE regions reaches ~ 100 nm order even above T_c .

B. Coherent x-ray scattering from paraelectric regions

Next, we focus on the *Bragg* reflection measured by CXS. As mentioned in Sec. II, the present CXS measurements were performed on cooling between 480 and 455 K in the PE phase.

Figures 10(a)–10(c) show selected CXS patterns taken at temperatures of 480, 462, and 456 K. So-called speckle patterns, aggregations of small spots, are clearly observed, indicating that the scattered x rays interfere with each other and therefore the patterns contain information on the texture of the PE regions in the irradiated area without averaging. We also show the speckle pattern from a perfect crystal (KTaO_3) in Fig. 10(d). As already presented in Ref. [13], if we irradiate a perfect crystal with no domains or defects, the CXS pattern will be a single spot (Bragg reflection in a real sense) as shown in Fig. 10(d). The spot size recorded on the CCD camera was about $18 \mu\text{m}$, which is in good agreement with the estimated value of $19 \mu\text{m}$ ($=\lambda R_2/a$). Figures 10(a')–10(d') show the results of Fourier transformation (FT) of the data in Figs. 10(a)–10(d), respectively. As shown in Appendix A, the FT of the speckle pattern gives the spatial autocorrelation function (S-ACF) of PE regions in the irradiated area. S-ACFs are often used to characterize the domain-domain correlation in ferroelectric materials [38–41].

Figure 11 shows one-dimensional (1D) patterns of the S-ACFs obtained from Figs. 10(a')–10(c') along the black dotted vertical lines. As can be seen in Fig. 3, the x-ray beam size on the sample (footprint) will be effectively about $30 \mu\text{m}$ in the horizontal direction at $2\theta \sim 40^\circ$, while it is exactly $10 \mu\text{m}$ in the vertical direction, which makes the analysis exact. The present spatial (\mathbf{r}') resolution was about 40 nm, which depends on the measurement area ($=$ momentum space) of the speckle pattern obtained using the present CCD camera.

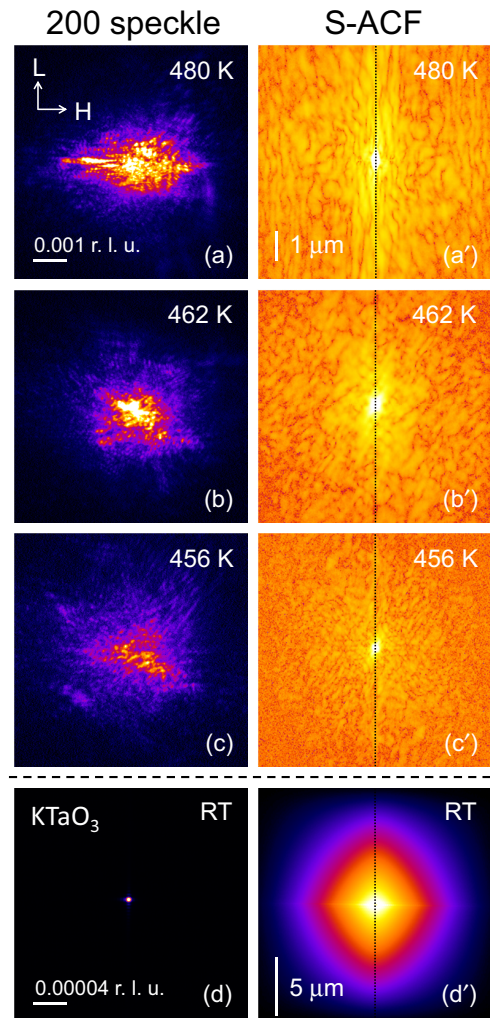


FIG. 10. (Color online) Selected CXS patterns taken at (a) 480 K, (b) 462 K, and (c) 456 K. (a')–(c') S-ACFs obtained from (a)–(c), respectively. Corresponding patterns from a perfect crystal (KTO_3) are also shown in (d) and (d').

As mentioned in Appendix B, the height of the central peak corresponds to the total volume of the PE regions contributing

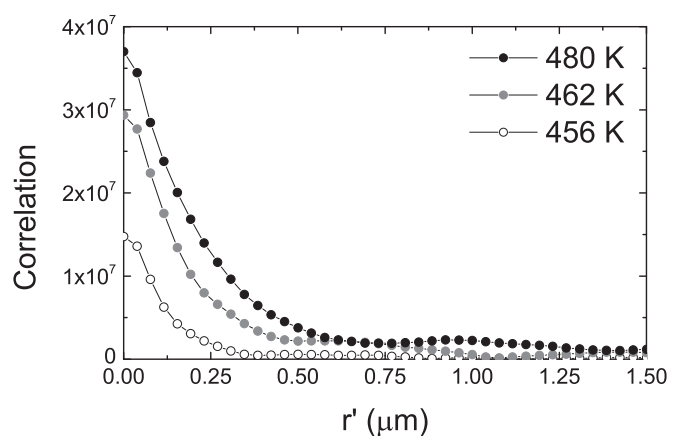
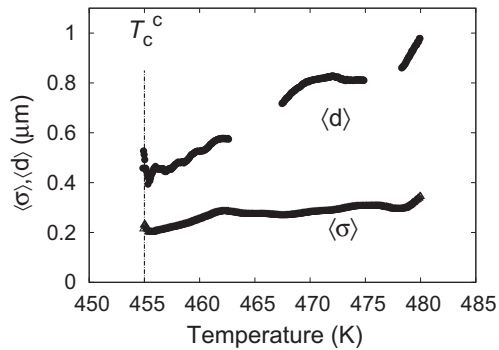


FIG. 11. One-dimensional patterns of S-ACFs obtained from Figs. 10(a')–10(c') along the black dotted vertical lines.


 FIG. 12. Temperature dependencies of $\langle\sigma\rangle$ and $\langle d\rangle$.

to the 200 Bragg reflection and is directly comparable to Fig. 7(a), the width of the central peak corresponds to the average size of the PE regions ($\langle\sigma\rangle$), and the position of the second peak corresponds to the average distance between neighboring PE regions ($\langle d\rangle$). We can see a decreasing trend for all these parameters.

Figure 12 shows the temperature dependencies of $\langle\sigma\rangle$ and $\langle d\rangle$ obtained from the 1D patterns. The average size of the PE regions decreases by about 2/3, and the average distance between the PE regions also decreases almost by half with decreasing temperature. The results also mean that the PE regions in the PE phase are spatially segmentalized by the appearance and increasing size of the FE regions on cooling. The trend continues to T_c^c , and $\langle\sigma\rangle$ and $\langle d\rangle$ finally reach about 200 and 400 nm, respectively.

Since we used a 10 μm coherent beam, a correlation longer than $\langle d\rangle$ among PE regions can be obtained. We plot all the 1D data below $r' = 5 \mu\text{m}$ as a function of temperature using contours as shown in Fig. 13. The lower panel shows all the data between 480 and 455 K, while the upper panel shows a magnification of the region between 460 and 455 K.

We can observe many “islands” in Fig. 13, corresponding to correlations among PE regions, and can clearly see that the correlations exist even at $r' = 5 \mu\text{m}$. The correlations gradually change as the temperature decreases and the rate of change rapidly increases below T_{max} , particularly near T_c^c . The temperature width of the islands, such as those labeled A, B, C, and D near 4 μm in Fig. 13, represents the duration of correlations among PE regions at the distance of 4 μm .

The duration of the correlations (ΔT) obtained from Fig. 13 is shown as a function of reduced temperature $[(T - T_c^c)/T_c^c]$ in Fig. 14. To obtain ΔT , the data were vertically integrated within 200 nm (for example, see the region sandwiched by the horizontal dashed lines near 4 μm in Fig. 13), and the 4 μm range was divided into 20 sections. ΔT is defined as the width between neighboring local minima (valley-peak-valley) as typically shown by the capped lines A–D in Fig. 13. The representative temperature corresponding to the obtained ΔT was determined as the midpoint between the two minima as shown in Fig. 13 by arrows.

As reported in Sec. II, the temperature interval of the present measurements was about 0.06 K. The minimum value of ΔT is 0.12 K, corresponding to the minimum valley-peak-valley period, and the subsequent values increase in steps of 0.06 K. Therefore, the resolution of the present measurements of ΔT

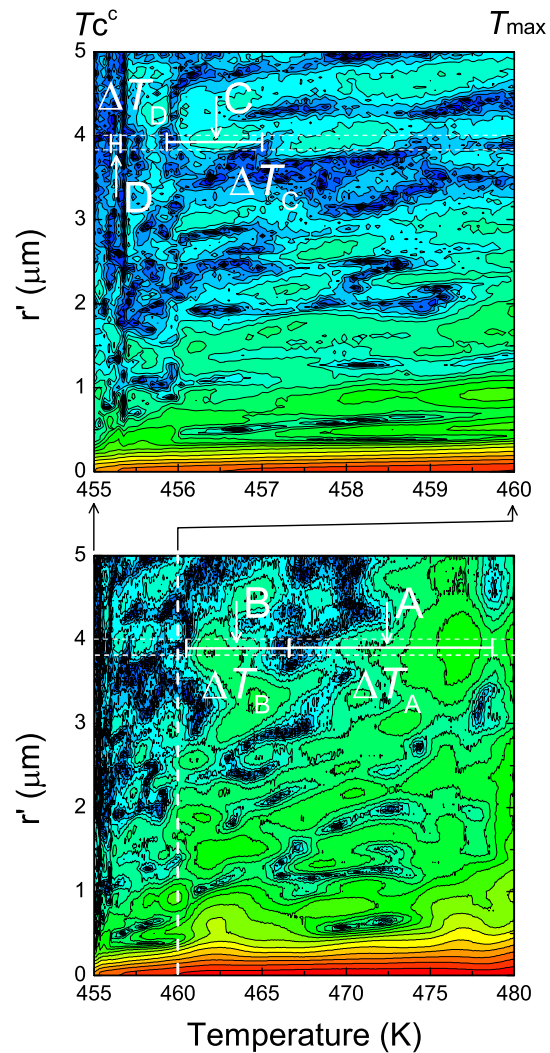
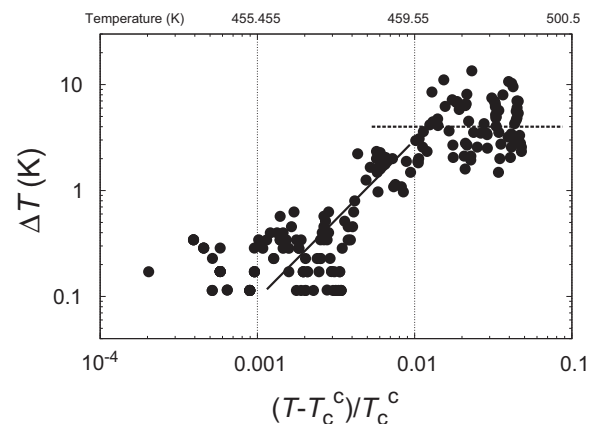


FIG. 13. (Color online) Contour plots of temperature vs S-ACF. The lower panel shows all the data between 480 and 455 K, while the upper panel shows a magnification of the region between 460 and 455 K. The temperature interval of the measurements was about 0.06 K.

is 0.12 K. This value is large compared with the resolution of temperature control achievable at the present stage of 0.04 K.


 FIG. 14. Temperature dependence of ΔT as a function of reduced temperature obtained from Fig. 13.

As shown in Fig. 14, the temperature dependence of ΔT is almost constant above T_{\max} [$(T - T_c^c)/T_c^c \sim 0.01$], while it rapidly decreases below T_{\max} toward T_c^c . As stated in Appendix B, the S-ACF clearly reflects the correlations among PE regions, i.e., the texture of the PE regions, in the PE phase contributing to the Bragg reflection at each angle of the crystal. However, the constant ΔT (see the dotted line in Fig. 14 given as a guide to the eye) above T_{\max} is understood as mainly resulting from extrinsic behavior. As shown in Fig. 4(a), the sample position along the scattering vector (shown as the S-K distance) continuously and constantly changes from 480 K to T_c^c . This change results in a change in the irradiated area on the sample, and therefore results in a change in the speckle patterns. The continuous and constant change in the speckle patterns results in a constant ΔT .

On the other hand, the rapid decrease below $\sim T_{\max}$ toward T_c^c (see the solid line in Fig. 14 given as a guide to the eye) cannot be explained by the continuous and constant change in the sample position. It can only originate from a dramatic change in the texture of the PE regions.

IV. HETEROPHASE FLUCTUATION

The results obtained from the two scattering measurements (XDS and CXS) can be summarized as follows. (i) The diffuse scattering intensities due to the appearance of FE regions have a maximum intensity at T_{\max} . The diffuse scattering is dynamic in nature and the softening trend changes to a hardening trend at T_{\max} . This means that the FE instability is maximum at T_{\max} and therefore the FE regions are well stabilized at T_{\max} . (ii) The S-ACF corresponding to the texture of the PE regions starts to rapidly change at about T_{\max} and is most unstable near T_c^c . (iii) Both XDS and CXS show that the PE regions in the PE phase are spatially segmentalized by the appearance and the stabilization of FE regions on cooling.

These results show that the FE regions become a semimacroscopic phase at T_{\max} and, at the same time, the texture of the PE regions starts to rapidly change. Therefore, the state of PZN-9%PT between T_{\max} and T_c^c is a so-called heterophase; semimacroscopic PE and FE phases coexist as if they are in a thermodynamic equilibrium state. As discussed in Sec. III A, the size of the FE regions is estimated to be larger than 20 nm, reaching a minimum size of the order of 100 nm, while the size of the PE regions (σ) is found to be about 200 nm from the S-ACF. The sizes of both regions are comparable to each other and strongly indicate the appearance of a heterophase state.

There should be many possible configurational patterns of semimacroscopic FE and PE regions in the heterophase state, and the patterns can be changed by a small temperature change, which can be clearly detected from the change in the S-ACF, as shown in Figs. 13 and 14. In this case, the physical quantity ΔT indicates the stability of the texture of the PE regions at the corresponding temperature. Therefore, in the heterophase state between T_{\max} and T_c^c , ΔT corresponds to the stability of the heterophase state.

The macroscopic phase transition of PZN-9%PT takes place at T_c^c , where the heterophase state is most unstable [$\Delta T \rightarrow 0$ (or a minimum)]. One of the most important indications of the present result is that the PE to FE phase

transition appears to receive a direct contribution from the fluctuation among semimacroscopic PE and FE regions as a precursor phenomenon of the first-order phase transition, which is a type of *heterophase fluctuation*. Note that the fluctuation of the phonon (ionic)-related microscopic system has already started hardening at 5 K above T_c^c . As shown in Fig. 1 and Ref. [13], a low-frequency dispersion is clearly observed between T_{\max} and T_c^c ; in addition, the frequency dispersion is greatest around T_c^c [13]. Therefore, the low-frequency dispersion can be considered to originate from the heterophase fluctuation.

Denoting the free energy of the high- and low-temperature phases of PZN-9%PT as F_H and F_L , respectively, we can naively consider that the first-order phase transition takes place when the free energy of both phases becomes equal ($F_H = F_L$). This situation should be realized at exactly T_c and therefore the heterophase state is allowed only at T_c . In practice, however, the heterophase state is realized at temperatures of over 5 K above T_c^c in PZN-9%PT. We thus have to consider contributions to the free energy originating from the heterophase.

The Ginzburg-Landau functional of the free energy can be introduced to accurately describe the heterophase state [10,42], where the spatially modulated order parameter (polarization in this case) can be introduced and the contribution of the *interface* (domain wall), given as a kink in the order parameter, can be considered. Gordon estimated the critical size of the pretransitional clusters (FE regions in this case) to be 140 nm for SbSI and stressed that the value for BaTiO₃ is comparable [42]. Actually, the heterophase was also observed in the FE material SbSI [43] within a narrow temperature range of less than 1 K near its transition temperature of 292 K. For the present PZN-9%PT, the obtained size of the regions is about 200 nm with a coexisting temperature range of 5 K, similarly to the results reported for conventional FE materials.

The correlation length of polar regions has been observed to decrease as the PT concentration decreases in the PM(Z)N- x %PT system. A neutron diffuse scattering study of the PMN- x %PT system [44] revealed that the correlation length decreases from about 35 nm (20%PT) to 1.3 nm (0%PT). The length scale of the heterogeneity changes from submicrometer to nanometer in the case of the PMN- x %PT system [44–46]. The present PZN- x %PT system can be understood similarly, and the *configurational entropy* should not be negligible near $x \sim 0\%$.

Finally, we mention the configurational entropy. First, a heterophase fluctuation in the gas-to-liquid phase transition was suggested by Frenkel by considering the configurational entropy [47]. The heterophase fluctuation in solids induced by the configurational entropy was also proposed to occur in Cu₃Au near the order-disorder transformation [48]. In these cases, a large number of states (configurations) are important.

The contribution of the configurational entropy [47,49] of the FE and PE regions to the free energy appears to be small in the case of PZN-9%PT. This is because the number of regions is much too small for them to contribute to the free energy in the case of a heterophase with 100 nm regions. Meanwhile, if we reduce the scale to the order of 1 nm so that the number of regions increases by a factor of 10^6 , the configurational entropy should not be negligible.

From the viewpoint of the interface, the elastic mismatch is small in a relaxor but large at a high PT concentration [50]. On the other hand, the configurational entropy is large in a relaxor ($x \sim 0\%$) but small at a high PT concentration as mentioned above. It is not clear at present how the size/scale of the regions in the PM(Z)N- $x\%$ PT system is determined, how the regions contribute to the physical properties, and whether or not a coherent fluctuation (collective mode) dominates the heterophase texture, i.e., something similar to the interactions among the interfaces of the heterophase, exists.

In any case, the excess entropy observed in a wide PT concentration range [50] suggests some contribution from higher-order structures and that the heterophase should be one of the origins of the excess entropy. Clarification of the contribution of the heterophase (or its interfaces) will be a key issue for elucidating the relaxor ferroelectrics [10,51].

V. SUMMARY

The PE to FE first-order phase transition of PZN-9%PT has been studied by the complementary use of XDS and CXS. XDS was mainly used to investigate the FE phase, while CXS was mainly used to investigate the PE phase. The diffuse scattering intensity due to the appearance of FE regions showed a maximum at T_{\max} . The diffuse scattering is dynamic in nature and the softening trend changes to a hardening trend at T_{\max} . This means that the FE instability is maximum at T_{\max} and therefore the FE regions are well stabilized below T_{\max} . The S-ACF obtained by CXS, corresponding to the texture of the PE regions, starts to rapidly change at about T_{\max} and is most unstable at T_c^c . We thus concluded that a heterophase fluctuation occurs between T_c^c and T_{\max} near the phase transition. The stability is expressed by ΔT . The heterophase fluctuation can be expected to correlate to the low-frequency dielectric dispersion and contribute to the phase transition as a precursor phenomenon of the first-order phase transition.

The present CXS technique is still under development; however, we consider that this report has demonstrated an advanced use of CXS for the study of heterogeneous solids. Since the coherent flux from the third-generation synchrotron sources is extremely low, the measurement was limited to the intense Bragg region. We hope that the *fluctuation* in solids can be observed in real time by CXS in the near future.

ACKNOWLEDGMENTS

We would like to express our gratitude to the following people for stimulating discussions and comments: Dr. H. Terauchi (Kwansei Gakuin University), Dr. M. Matsuura, Dr. Y. Fujii (CROSS-Tokai), Dr. S. Tsukada (Shimane University), Dr. M. Iwata (Nagoya Institute of Technology), Dr. H. Nakao, Dr. Y. Murakami (IMSS-KEK), Dr. S. Shimomura (Kyoto Sangyo University), Dr. E. Matsushita (Gifu University), Dr. J. Harries (JAEA), the late Dr. K. Hirota (Osaka University), and the late Dr. G. Shirane (Brookhaven National Laboratory). This work was partly supported by a Grant-in-Aid for Scientific Research on Priority Areas ‘‘Novel States of Matter Induced by Frustration’’ (Grant No. 19052002) and Grants-in-Aid for Young Scientists(B) (Grants No. 16740177 and No. 21710099). The synchrotron radiation experiments

were performed at BL22XU of SPring-8 with the approval of Japan Synchrotron Radiation Research Institute (JASRI) (Proposals No. 2011B3713, No. 2011A3713, No. 2010B3713, No. 2010A3713, No. 2009B3713, and No. 2009A3713).

APPENDIX A: GENERAL FRAMEWORK FOR X-RAY SCATTERING USED IN THIS WORK

1. Bragg reflection and diffuse scattering

a. Homogeneous systems

If we give the electron density of a solid as a function of position (\mathbf{r}) and time (t) as $\rho(\mathbf{r}, t)$, the x-ray scattering intensity (I) can be expressed using the autocorrelation function of $\rho(\mathbf{r}, t)$ as

$$I = \mathcal{F}\{\langle \rho(\mathbf{r}, t) \rho(\mathbf{r} + \mathbf{r}', t + t') \rangle_{\mathbf{r}, t}\}, \quad (\text{A1})$$

where $\mathcal{F}\{\}$ represents the Fourier transform of space (\mathbf{r}') and time (t'), and $\langle \rangle_{\mathbf{r}, t}$ denotes the ensemble average over \mathbf{r} and t .

If we suppose that the electron density of a solid $\rho(\mathbf{r}, t)$ can be rewritten using the average electron density $[\overline{\rho(\mathbf{r})}]$ and the deviation from the average electron density $[\Delta\rho(\mathbf{r}, t)]$ as

$$\rho(\mathbf{r}, t) = \overline{\rho(\mathbf{r})} + \Delta\rho(\mathbf{r}, t), \quad (\text{A2})$$

then the x-ray scattering intensity can be rewritten as

$$I = \mathcal{F}\{\langle \overline{\rho(\mathbf{r})} \overline{\rho(\mathbf{r} + \mathbf{r}')}\rangle_{\mathbf{r}}\} + \mathcal{F}\{\langle \Delta\rho(\mathbf{r}, t) \Delta\rho(\mathbf{r} + \mathbf{r}', t + t') \rangle_{\mathbf{r}, t}\}. \quad (\text{A3})$$

The first term represents the *Bragg* reflection intensity (I_B) and the second term represents the diffuse scattering intensity (I_D). The Bragg reflection closely reflects the average structure of solids (the PE regions in this paper), while the diffuse scattering closely reflects the spatial and time fluctuation of solids (the FE regions in this paper).

b. Heterogeneous systems

In the case of a heterophase structure, the above treatment can also basically be applied. Figure 15 shows a schematic drawing of the heterophase structure of a solid, where the structure consists of many regions. We index the regions as i , $i + 1$, and so forth. Then, the sectional electron densities are defined as $\rho_i(\mathbf{r}, t)$, $\rho_{i+1}(\mathbf{r}, t)$, and so forth. Since each region is uniform, the electron density of each region (i) can be rewritten as

$$\rho_i(\mathbf{r}, t) = \overline{\rho_i(\mathbf{r})} + \Delta\rho_i(\mathbf{r}, t) \quad (\text{A4})$$

(see the examples in Fig. 15). Using this expression, we can redefine the average density of the heterophase as

$$\overline{\rho_{\text{hetero}}(\mathbf{r})} [= \overline{\rho(\mathbf{r})}] = \sum_i \overline{\rho_i(\mathbf{r})}, \quad (\text{A5})$$

where the summation should be performed coherently, i.e., all the average densities $[\overline{\rho_i(\mathbf{r})}]$ have the same origin. In this paper, we call the density $\overline{\rho(\mathbf{r})}$ the *overall* density instead of the average density in the case of the heterophase.

Note that in conventional textbooks on x-ray scattering, Bragg reflection is expressed by assuming a homogeneous system with a lattice constant a_0 . In this case, extremely strong scattering occurs at the center of the scattering profile as shown in Fig. 10(d).

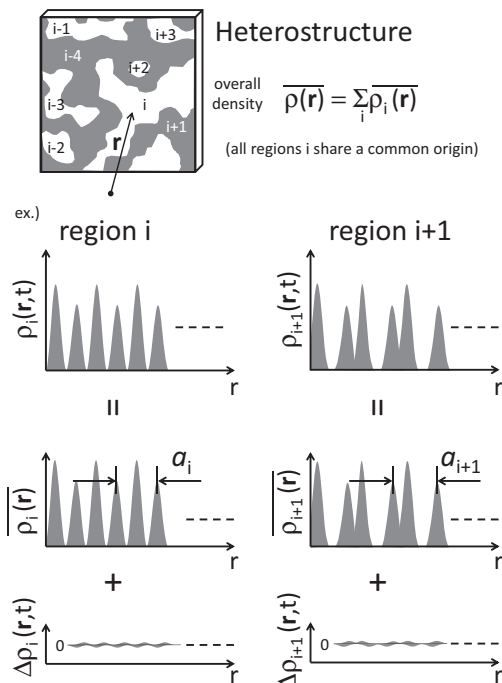


FIG. 15. Schematic drawing of the heterophase structure of a solid. The heterophase structure consists of many regions indexed as i , $i + 1$, and so forth. The electron density of each region $[\rho_i(\mathbf{r}, t)]$ can be separated into $\overline{\rho_i(\mathbf{r})} + \Delta\rho_i(\mathbf{r}, t)$. The coherent sum of $\overline{\rho_i(\mathbf{r})}$ (overall density) contributes to the so-called speckle pattern of Bragg reflection.

However, generally in the heterogeneous case, as shown in the examples in Fig. 15, each region has its own lattice constant a_i . The difference in the lattice constant among the regions results in a speckle pattern as shown in Figs. 10(a)–10(c). In this paper, the scattering originating from Eq. (A5) is also treated as Bragg reflection.

A realistic interpretation of the observed speckle pattern and the related overall densities is given in Appendix B 3.

2. Partially coherent x-ray scattering (realistic x-ray scattering)

Up to this point, the incident x rays have been assumed to be coherent. However, most x-ray sources provide *partially coherent* x rays to various degrees [52]. Therefore, we have to consider the (normalized) mutual coherence function $[\gamma_{\mathbf{r}, \mathbf{r}+\mathbf{r}'}(t')]$ between diffracted wave fields, which is renormalized into that between electron densities in the formalism of the Fourier transform [Eq. (A1)]. Details and a precise treatment are given in Ref. [52]. Using $\gamma_{\mathbf{r}, \mathbf{r}+\mathbf{r}'}(t')$, Eq. (A1) can be rewritten as

$$I = \mathcal{F}\{\langle \gamma_{\mathbf{r}, \mathbf{r}+\mathbf{r}'}(t') \rho(\mathbf{r}, t) \rho(\mathbf{r} + \mathbf{r}', t + t') \rangle_{\mathbf{r}, t}\}, \quad (\text{A6})$$

where $\gamma_{\mathbf{r}, \mathbf{r}+\mathbf{r}'}(t')$ should be 1 when $\mathbf{r}' = 0$. When $\mathbf{r}' \neq 0$, the degree of coherence is given as

$$\begin{aligned} |\gamma_{\mathbf{r}, \mathbf{r}+\mathbf{r}'}| &= 1 \text{ (coherent),} \\ |\gamma_{\mathbf{r}, \mathbf{r}+\mathbf{r}'}| &= 0 \text{ (incoherent),} \\ 0 &< |\gamma_{\mathbf{r}, \mathbf{r}+\mathbf{r}'}| < 1 \text{ (partially coherent).} \end{aligned} \quad (\text{A7})$$

The commonly used term “x-ray scattering” refers to the case of using partially coherent x rays.

3. Coherent x-ray scattering

A major advantage of the present CXS is that we can use x rays close to the coherent condition ($|\gamma_{\mathbf{r}, \mathbf{r}+\mathbf{r}'}| \sim 1$), allowing Eq. (A6) to be rewritten as

$$\begin{aligned} I &= \mathcal{F}\{\langle \gamma_{\mathbf{r}, \mathbf{r}+\mathbf{r}'} \rho(\mathbf{r}, t) \rho(\mathbf{r} + \mathbf{r}', t + t') \rangle_{\mathbf{r}, t}\} \\ &\sim \mathcal{F}\{\langle \rho(\mathbf{r}, t) \rho(\mathbf{r} + \mathbf{r}', t + t') \rangle_{\mathbf{r}, t}\}. \end{aligned} \quad (\text{A8})$$

If we consider a time-averaged heterogeneous solid with a characteristic length scale of the heterogeneity (v) within the volume “coherently” irradiated by x rays (V_c) ($v < V_c$), the coherent sum of scattered x rays from the solid having a heterogeneous structure results in a so-called *speckle* pattern. The speckle pattern contains information on not only components of the heterogeneous structure $[\rho_i(\mathbf{r}, t)]$, such as domains, but also the heterogeneous structure itself $[\sum_i \rho_i(\mathbf{r}, t)]$.

Changes in the heterogeneous structure result in fine changes in the speckle pattern. A Fourier transformation of the speckle pattern gives the S-ACF of the solid. This enables us to visualize the heterogeneous structure and the arrangement of the components through an autocorrelation function.

Under an almost incoherent condition ($v \gg V_c$), the speckle pattern disappears and a well-averaged overall profile can be observed. This type of scattering pattern can usually be seen when using a laboratory light source.

APPENDIX B: SPATIAL AUTOCORRELATION FUNCTION

1. Case of a perfect crystal

For the present CXS experiment, the spatial (\mathbf{r}') resolution was about 40 nm, about 100 times larger than the perovskite unit cell. As already discussed in Sec. III B, this is due to the limitation of the measurement area (=momentum space) of the speckle pattern for the present CCD camera [$\Delta q \sim 0.01$ (r.l.u.)]. On the basis of this condition, in the case of a homogeneous and perfect crystal, we can assume that the average electron density $\overline{\rho(\mathbf{r})}$ is constant, $\overline{\rho(\mathbf{r})} = \rho_0$, as shown in Fig. 16(a). If we irradiate the crystal with coherent x rays with a size of b , the autocorrelation function will be given as shown in Fig. 16(b), with a monotonic decrease to zero at $r' = b$. Figure 16(c) is obtained from Fig. 10(d'), and the shape is ideal for the case of a perfect crystal.

2. Heterogeneous case: Minimal model of PZN-9%PT

In this section, we describe the primitive method of analyzing the S-ACF employed in this work. References [38,39] are extensively referred to here.

In our measurements, as frequently stressed, the S-ACF from the speckle pattern originated from the 200 Bragg reflection of the PE phase. We suppose that the PE regions are distributed in the x-ray-irradiated area (b^2) and the interspaces among the PE regions are filled by newly appearing FE regions as shown in Fig. 17(a). We also assume that the average density of each PE region is constant for the same reason as discussed

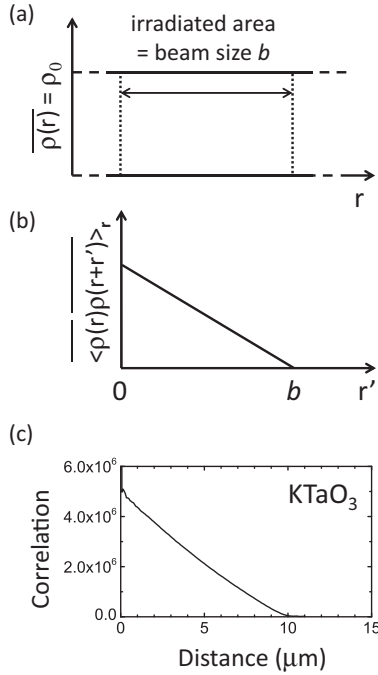


FIG. 16. (a) The average electron density $\overline{\rho(r)}$ can be assumed constant, $\overline{\rho(r)} = \rho_0$, in the present CXS measurement. An x ray with a size of b is irradiated. (b) S-ACF obtained from (a). (c) One-dimensional pattern of S-ACF obtained from Fig. 10(d'). An ideal triangular graph can be seen.

for the case of a perfect crystal. The size of the PE regions and the distances between them are given as σ_i and d_i , respectively. The local fluctuation giving $\Delta\rho(\mathbf{r}, t)$ can be ignored in this analysis.

Figure 17(b) is a schematic drawing of the S-ACF obtained from the electron density of the PE regions shown in Fig. 17(a).

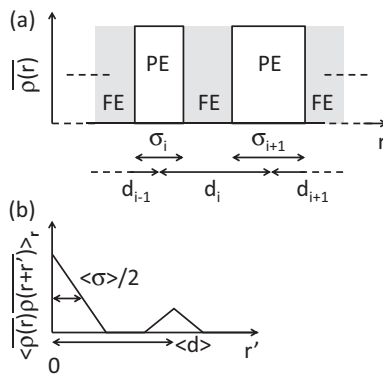


FIG. 17. Minimal model of PE phase of PZN-9%PT used for understanding of the S-ACF obtained from CXD. (a) Schematic diagram of PZN-9%PT. The PE regions are distributed in the x-ray-irradiated area and the interspaces among the PE regions are filled by newly appearing FE regions. σ_i are the sizes of the PE regions, while d_i are the distances between the PE regions. (b) Schematic drawing of S-ACF obtained from (a). The width of the central peak represents the average size of the PE regions $\langle\sigma\rangle$, while the distance between the center and the nearest peak represents the average distance between neighboring PE regions $\langle d\rangle$.

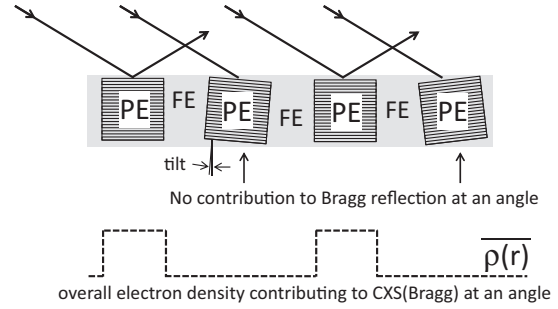


FIG. 18. Meaning of the overall density. Not all PE regions contribute to the Bragg reflection at an angle.

The width of the central peak represents the average size of the PE regions (σ), while the distance between the center and the nearest-neighbor peak represents the average distance between neighboring PE regions (d).

3. Meaning of the overall density

In the case of conventional x-ray scattering from crystals, we rarely consider the *overall* density. In the present case, the bulk of the PE phase is segmentalized by the newly appearing FE regions. The symmetry of the FE regions is not cubic (tetragonal symmetry or lower) and the sizes are not negligible. The appearance of the FE regions results in the destruction of the coherence among the PE regions and, furthermore, the PE regions are slightly tilted by the appearance of the FE regions as shown in Fig. 18. These phenomena cause peak broadening as shown in Fig. 4(b). In the present CXS measurement, the angle ω is fixed at near the center. In this case, the CXS only detects the PE regions contributing to the reflection at the angle. The heights of the central peak of the obtained S-ACF ($=\langle\overline{\rho(r)}^2\rangle$) correspond to the total volume of PE regions contributing to the 200 Bragg reflection at the angle.

The peak intensity of the S-ACF at the distance $\langle d\rangle$ corresponds to the probability of finding PE regions separated by a distance of $\langle d\rangle$ and also corresponds to the density of PE regions contributing to the Bragg reflection at an angle.

By a simple consideration, the percentage by volume of the PE regions contributing to the Bragg reflection at an angle can be expressed as follows:

$$\frac{\langle\sigma\rangle}{\langle d\rangle} \frac{I_{1st}}{I_{cen}}, \quad (\text{B1})$$

where I_{cen} and I_{1st} represent the central peak and the peak closest to the central peak of the S-ACF, respectively. The correction of the monotonic reduction of the S-ACF, as shown in Fig. 16(b), is not considered here. From the data of Figs. 11 and 12, we can understand that only a few percent by volume of PE regions contributes to the CXS pattern when the angle ω is set at the center of the rocking curve near T_c^c . This is consistent with the ratio between the rocking curve width [about 0.1° ; see Fig. 4(b)] and the incident x-ray divergence [6 arcsec $\sim 0.00167^\circ$, the Darwin width of Si(111)]. This is one of the reasons why we have to consider the overall density, not the simple average density, in the case of CXS measurements of heterogeneous systems.

- [1] G. A. Smolenskii and A. I. Agronovskaya, *Sov. Phys. Tech. Phys. A* **3**, 1380 (1958).
- [2] Y. Yamada, T. Iwase, K. Fujishiro, Y. Uesu, Y. Yamashita, I. Tomeno, and S. Shimanuki, *Ferroelectrics* **240**, 1629 (2000).
- [3] D. Fu, H. Taniguchi, M. Itoh, S.-y. Koshihara, N. Yamamoto, and S. Mori, *Phys. Rev. Lett.* **103**, 207601 (2009).
- [4] G. Burns and F. H. Dacol, *Solid State Commun.* **48**, 853 (1983).
- [5] G. Burns and F. H. Dacol, *Phys. Rev. B* **28**, 2527 (1983).
- [6] Y. Tokura, *Rep. Prog. Phys.* **69**, 797 (2006).
- [7] S. Wada, S.-E. Park, L. E. Cross, and T. R. ShROUT, *J. Korean Phys. Soc.* **32**, S1290 (1998).
- [8] S.-E. Park and T. R. ShROUT, *J. Appl. Phys.* **82**, 1804 (1997).
- [9] S. Wada, K. Yako, H. Kakemoto, J. Erhart, and T. Tsurumi, *Key Eng. Mater.* **269**, 19 (2004).
- [10] M. Iwata and Y. Ishibashi, *Jpn. J. Appl. Phys.* **51**, 09LE03 (2012).
- [11] Z. Kutnjak, J. Petzelt, and R. Blinc, *Nature (London)* **441**, 956 (2006).
- [12] M. Iwata, S. Kato, and Y. Ishibashi, *Ferroelectrics* **415**, 20 (2011).
- [13] K. Ohwada, J. Mizuki, K. Namikawa, M. Matsushita, S. Shimomura, H. Nakao, and K. Hirota, *Phys. Rev. B* **83**, 224115 (2011).
- [14] S. Brauer, G. B. Stephenson, M. Sutton, R. Brünig, E. Dufresne, S. G. J. Mochrie, G. Grübel, J. Als-Nielsen, and D. L. Abernathy, *Phys. Rev. Lett.* **74**, 2010 (1995).
- [15] S. B. Dierker, R. Pindak, R. M. Fleming, I. K. Robinson, and L. Berman, *Phys. Rev. Lett.* **75**, 449 (1995).
- [16] J. Miao, P. Charalambous, J. Kirz, and D. Sayre, *Nature (London)* **400**, 342 (1999).
- [17] R. H. I. Robinson, *Nat. Mater.* **8**, 291 (2009).
- [18] M. Matsushita, Y. Tachi, and K. Echizenya, *J. Cryst. Growth* **237–239**, 853 (2002).
- [19] T. Shobu, K. Tozawa, H. Shiwaku, H. Konishi, T. Inami, T. Harami, and J. Mizuki, *Synchrotron Radiation Instrumentation: Ninth International Conference on Synchrotron Radiation Instrumentation*, AIP Conf. Proc. No. 879 (AIP, Melville, NY, 2007), p. 902.
- [20] M. Sutton, S. G. J. Mochrie, T. Greytak, S. E. Nagler, L. E. Berman, G. A. Held, and G. B. Stephenson, *Nature (London)* **352**, 608 (1991).
- [21] K. Ohwada, K. Namikawa, J. Mizuki, S. Shimomura, H. Nakao, K. Ito, M. Matsushita, Y. Yoneda, Y. Murakami, and K. Hirota, *Trans. Mater. Res. Soc. Jpn.* **32**, 7 (2007).
- [22] M. D. Abramoff, P. J. Magelhaes, and S. J. Ram, *Biophotonics Int.* **11**, 36 (2004).
- [23] R. J. Birgeneau, J. K. Kjems, G. Shirane, and L. G. Van Uiter, *Phys. Rev. B* **10**, 2512 (1974).
- [24] K. Hirota, Z.-G. Ye, S. Wakimoto, P. M. Gehring, and G. Shirane, *Phys. Rev. B* **65**, 104105 (2002).
- [25] S. Wakimoto, C. Stock, R. J. Birgeneau, Z.-G. Ye, W. Chen, W. J. L. Buyers, P. M. Gehring, and G. Shirane, *Phys. Rev. B* **65**, 172105 (2002).
- [26] S. Wakimoto, C. Stock, Z.-G. Ye, W. Chen, P. M. Gehring, and G. Shirane, *Phys. Rev. B* **66**, 224102 (2002).
- [27] G. Xu, P. M. Gehring, and G. Shirane, *Phys. Rev. B* **74**, 104110 (2006).
- [28] Z. Xu, J. Wen, G. Xu, C. Stock, J. S. Gardner, and P. M. Gehring, *Phys. Rev. B* **82**, 134124 (2010).
- [29] C. Stock, P. M. Gehring, H. Hiraka, I. Swainson, G. Xu, Z.-G. Ye, H. Luo, J.-F. Li, and D. Viehland, *Phys. Rev. B* **86**, 104108 (2012).
- [30] Y. Terado, S. J. Kim, C. Moriyoshi, Y. Kuroiwa, M. Iwata, and M. Takata, *Jpn. J. Appl. Phys.* **45**, 7552 (2006).
- [31] Y. Uesu, H. Tazawa, K. Fujishiro, and Y. Yamada, *J. Korean Phys. Soc.* **29**, S703 (1996).
- [32] Y. Yamada and T. Takakura, [arXiv:cond-mat/0209573](https://arxiv.org/abs/cond-mat/0209573).
- [33] A. Bosak, D. Chernyshov, S. Vakhrushev, and M. Krisch, *Acta Crystallogr. A* **68**, 117 (2012).
- [34] M. Paściak, T. R. Welberry, J. Kulda, M. Kempa, and J. Hlinka, *Phys. Rev. B* **85**, 224109 (2012).
- [35] Y. Yamada, H. Takatera, and D. L. Huber, *J. Phys. Soc. Jpn.* **36**, 641 (1974).
- [36] P. M. Gehring, H. Hiraka, C. Stock, S.-H. Lee, W. Chen, Z.-G. Ye, S. B. Vakhrushev, and Z. Chowdhuri, *Phys. Rev. B* **79**, 224109 (2009).
- [37] M. Matsuura, H. Hiraka, K. Yamada, and K. Hirota, *J. Phys. Soc. Jpn.* **80**, 104601 (2011).
- [38] V. V. Shvartsman and A. L. Kholkin, *J. Appl. Phys.* **101**, 064108 (2007).
- [39] R. Z. Tai, K. Namikawa, M. Kishimoto, M. Tanaka, K. Sukegawa, N. Hasegawa, T. Kawachi, M. Kado, P. Lu, K. Nagashima *et al.*, *Phys. Rev. Lett.* **89**, 257602 (2002).
- [40] R. Z. Tai, K. Namikawa, A. Sawada, M. Kishimoto, M. Tanaka, P. Lu, K. Nagashima, H. Maruyama, and M. Ando, *Phys. Rev. Lett.* **93**, 087601 (2004).
- [41] V. V. Shvartsman, W. Kleemann, T. Łukasiewicz, and J. Dec, *Phys. Rev. B* **77**, 054105 (2008).
- [42] A. Gordon, *J. Phys. C: Solid State Phys.* **20**, L111 (1987).
- [43] T. Mori, H. Tamura, and E. Sawaguchi, *J. Phys. Soc. Jpn.* **20**, 1294 (1965).
- [44] M. Matsuura, K. Hirota, P. M. Gehring, Z.-G. Ye, W. Chen, and G. Shirane, *Phys. Rev. B* **74**, 144107 (2006).
- [45] V. V. Shvartsman and A. L. Kholkin, *Phys. Rev. B* **69**, 014102 (2004).
- [46] F. Bai, J. Li, and D. Viehland, *J. Appl. Phys.* **97**, 054103 (2005).
- [47] J. Frenkel, *J. Chem. Phys.* **7**, 538 (1939).
- [48] P. Bardhan, H. Chen, and J. B. Cohen, *Philos. Mag.* **35**, 1653 (1977).
- [49] D. D. Fontaine, *Acta Metall.* **23**, 553 (1975).
- [50] M. Tachibana, K. Sasame, H. Kawaji, T. Atake, and E. Takayama-Muromachi, *Phys. Rev. B* **80**, 094115 (2009).
- [51] J. Hlinka, *J. Adv. Dielect.* **02**, 1241006 (2012).
- [52] K. A. Nugent, *Adv. Phys.* **59**, 1 (2010).